Domain alignment within ferroelectric/dielectric PbTiO$_3$/SrTiO$_3$ superlattice nanostructures: Supporting information

Joonkyu Park,[†] John Mangeri,[‡] Qingteng Zhang,[†] Mohammed Humed Yusuf,[¶] Anastasios Pateras,[†] Matthew Dawber,[¶] Martin V. Holt,[§] Olle G. Heinonen,[‖,⊥] Serge Nakhmanson,[#,‡] and Paul G. Evans[*,†]

[†]*Department of Materials Science & Engineering, University of Wisconsin-Madison, Madison, Wisconsin 53706, USA*

[‡]*Department of Physics, University of Connecticut, Storrs, Connecticut 06269, USA*

[¶]*Department of Physics and Astronomy, Stony Brook University, Stony Brook, New York 11794, USA*

[§]*Center for Nanoscale Materials, Argonne National Laboratory, Lemont, Illinois 60439, USA*

[‖]*Material Science Division, Argonne National Laboratory, Lemont, Illinois 60439, USA*

[⊥]*Center for Hierarchical Material Design, Northwestern-Argonne Institute of Science and Engineering, Northwestern University, Evanston, Illinois 60208, USA*

[#]*Department of Materials Science & Engineering and Institute of Material Science, University of Connecticut, Storrs, Connecticut 06269, USA*

E-mail: pgevans@wisc.edu

Here we summarize the methods used to calculate the coupled polar-elastic energies of the ferroelectric/dielectric superlattice nanostructure and describe the details of the structural analysis

using x-ray nanodiffraction.

1. Methods

1.1. System energies

The total free energy, F_{total}, of a ferroelectric (FE) $PbTiO_3$ (PTO) structure can be written as a linear combination of the energies[1,2] from different contributions as

$$F_{\text{total}} = \int_V f \, d^3\mathbf{x} = \int_V [f_{\text{bulk}} + f_{\text{electrostatic}} + f_{\text{wall}} + f_{\text{elastic}} + f_{\text{coupled}}] d^3\mathbf{x}, \tag{1}$$

with an integration over the computational domain V. Spatial variables are defined in Cartesian coordinates as $\mathbf{x} = \langle x_1, x_2, x_3 \rangle$. The term

$$\begin{aligned} f_{\text{bulk}} = {}& \alpha_1(T) \left(P_1^2 + P_2^2 + P_3^2 \right) + \alpha_{11} \left(P_1^4 + P_2^4 + P_3^4 \right) \\ & + \alpha_{12} \left(P_1^2 P_2^2 + P_2^2 P_3^2 + P_1^2 P_3^2 \right) + \alpha_{111} \left(P_1^6 + P_2^6 + P_3^6 \right) \\ & + \alpha_{112} \left[P_1^4 \left(P_2^2 + P_3^2 \right) + P_2^4 \left(P_1^2 + P_3^2 \right) + P_3^4 \left(P_1^2 + P_2^2 \right) \right] \\ & + \alpha_{123} \left(P_1^2 P_2^2 P_3^2 \right), \end{aligned} \tag{2}$$

corresponds to the bulk free energy density depending on the spatial varying polarization field $\mathbf{P}(\mathbf{x}) = \langle P_1(\mathbf{x}), P_2(\mathbf{x}), P_3(\mathbf{x}) \rangle$. The minima of f_{bulk} determine the preferred directions and magnitudes of P in the unit cell at a given temperature T below T_C. The energetic approach includes $f_{\text{electrostatic}} = -\mathbf{P} \cdot \nabla \Phi$, where $\Phi(\mathbf{x})$ is the spatially dependent electrostatic potential. This contribution to the total energy represents the interaction of the FE polarization with internal and external electric fields. The term f_{wall} expresses the energy contributions arising from *local* gradients as the

polarization exchange coupling between domains across the domain wall. For the given material (PTO),

$$f_{\text{wall}} = \frac{1}{2}G_{11}\left[\left(\frac{\partial P_1}{\partial x_1}\right)^2 + \left(\frac{\partial P_2}{\partial x_2}\right)^2 + \left(\frac{\partial P_3}{\partial x_3}\right)^2\right] \tag{3}$$
$$+ G_{12}\left[\frac{\partial P_1}{\partial x_1}\frac{\partial P_2}{\partial x_2} + \frac{\partial P_2}{\partial x_2}\frac{\partial P_3}{\partial x_3} + \frac{\partial P_1}{\partial x_1}\frac{\partial P_3}{\partial x_3}\right]$$
$$+ \frac{1}{2}G_{44}\left[\left(\frac{\partial P_1}{\partial x_2} + \frac{\partial P_2}{\partial x_1}\right)^2 + \left(\frac{\partial P_2}{\partial x_3} + \frac{\partial P_3}{\partial x_2}\right)^2 + \left(\frac{\partial P_1}{\partial x_3} + \frac{\partial P_3}{\partial x_1}\right)^2\right]$$
$$+ \frac{1}{2}G_{44}'\left[\left(\frac{\partial P_1}{\partial x_2} - \frac{\partial P_2}{\partial x_1}\right)^2 + \left(\frac{\partial P_2}{\partial x_3} - \frac{\partial P_3}{\partial x_2}\right)^2 + \left(\frac{\partial P_1}{\partial x_3} - \frac{\partial P_3}{\partial x_1}\right)^2\right].$$

The problem is coupled to elasticity through two energetic terms. The linear elastic free energy $f_{\text{elastic}} = \frac{1}{2}C_{ijkl}(\varepsilon_{ij} - \varepsilon_{ij}^0)(\varepsilon_{kl} - \varepsilon_{ij}^0)$ accounts for linear elastic strain contributions to the total energy, with C_{ijkl} being the elastic stiffness tensor, and ε_{ij}^0 the eigenstrain, which in our case is the stress-free strain that arises from the polarization. The elastic strain tensor is represented by $\varepsilon_{ij} = \frac{1}{2}\left(\partial u_i/\partial x_j + \partial u_j/\partial x_i\right)$ with $\mathbf{u}(\mathbf{r})$ being the displacement vector field. The strain is then coupled to the polarization with the f_{coupled} term, which is expressed linear in the strain and quadratic in the polarization,

$$f_{\text{coupled}} \equiv \frac{1}{2}q_{ijkl}\varepsilon_{ij}P_kP_l, \tag{4}$$

where $q_{ijkl} = 2\,Q_{ijmn}C_{mnkl}$ is the electrostrictive tensor. For the above expressions, the Einstein summation convention is assumed for repeated indices. Note that some works in the literature (for example 1 and 2) combine f_{elastic} and f_{coupled} into one term. Here, we have chosen to separate them because the result of the variational differentiation (with respect to $\boldsymbol{P}$) in the time-dependent Landau-Ginzburg-Devonshire equations, to be discussed in the next few sections, will only give

3

nonzero results for terms that explicitly contain $\boldsymbol{P}$.

1.2. Materials parameters

For the bulk free energy that describes the energetics of the phase transition, only sixth order expansions are used, which is sufficient to reproduce the behavior of PTO within the temperature range considered here.[3] The coefficients for the bulk free energy contributions are listed in Table 1. We also set $G_{110} = 1.73$, $G_{11}/G_{110} = 0.6$, $G_{12}/G_{110} = 0.0$, and $G_{44}/G_{110} = G'_{44}/G_{110} = 0.3$ in units of $10^{-10}\mathrm{C}^{-2}\mathrm{m}^4\mathrm{N}$.[1,2]

We assume an isotropic (and linear) dielectric medium for the $\mathrm{SrTiO_3}$ (STO) substrate and vacuum region. The STO substrate is also treated as elastic and coherently connected to the ferroelectric region. The elastic stiffness tensor parameters listed in Table 2 are presented in Voight notation.[4] For the STO substrate, the elastic constants were averaged as $C_{11,} = C_{33} = 2\mu + \lambda$, $C_{12} = C_{13} = \lambda = 99.7$ GPa, and $C_{44} = C_{66} = \mu = 109.6$ GPa,[5,6] which is a reasonable experimentally relevant assumption, since the substrate elastic anisotropy is low.

Table 1: Ferroelectric material parameters used in this work for $\mathrm{PbTiO_3}$ at room temperature, $T = 293$ K. Elastic stiffness and electrostrictive tensor coefficients are given in Voight notation.[4] Sixth-order expansions of the bulk free energy are used for both materials. All coefficients are given in SI units.

	$\mathrm{PbTiO_3}$	Ref.
α_1	-7.1×10^7	7
α_{11}	-7.3×10^7	-
α_{12}	7.5×10^8	-
α_{111}	2.6×10^8	-
α_{112}	6.1×10^8	-
α_{123}	-3.7×10^9	-
ϵ_b	10	
Q_{11}	0.089	1
Q_{12}	-0.026	-
Q_{33}	0.034	-
C_{11}	281	5,6
C_{12}	116	-
C_{33}	97	-

Table 2: Linear dielectric material parameters used in this work for $SrTiO_3$ at room temperature, $T = 293$ K. Medium dielectric constants are assumed to be isotropic and are given in units of the relative permittivity. Elastic stiffness tensor coefficients are given in Voight notation[4] in units of GPa.

	$SrTiO_3$	vacuum	Ref
C_{11}	319	-	5,6
C_{12}	100	-	-
C_{44}	110	-	-
ϵ_m/ϵ_0	300	1	8

1.3. Relaxational approach

FERRET[9] is an open-source package for modeling ferroelectric nanostructures based on the multiphysics finite element framework MOOSE.[10] The evolution of the polarization field, $\boldsymbol{P}$, in the ferroelectric layer is described by the time-dependent Landau-Ginzburg-Devonshire (TDLGD) equation,

$$- \gamma\frac{\partial \boldsymbol{P}}{\partial t} = \frac{\delta}{\delta \boldsymbol{P}} \int\limits_{V} f\left(\boldsymbol{P}\right) \, d^3\mathbf{x}, \tag{5}$$

where γ is a time-scaling parameter related to domain-wall mobility.[11] The variable γ is set to unity in this investigation and, therefore, the TDLGD equation is evolved in an arbitrary scaled time. This assumption is due to the fact that in real FE materials and structures, elastic strain usually relaxes much faster than the polarization,[12] we assume that the local displacement field $\mathbf{u}(\mathbf{x})$ instantaneously adjusts to the current state of the polarization field $\boldsymbol{P}$. This results in the following mechanical equilibrium condition for the system that must be satisfied at every time step of the evolution of $\boldsymbol{P}$:

$$\frac{\partial}{\partial x_j} \left[C_{ijkl}\left(\varepsilon_{kl} - Q_{ijmn}P_m P_n \right) \right] = 0, \tag{6}$$

where the second term is the *eigenstrain* that arises from the coupling of the polarization to the elastic strain.[1] Furthermore, the evolution of $\boldsymbol{P}$ is also coupled with that of the local (internal)

electrostatic potential Φ by the Poisson equation:

$$\nabla \cdot (\epsilon_b \nabla \Phi) = -\rho_b. \tag{7}$$

Here, ρ_b is bound volume charge equal to $\nabla \cdot \boldsymbol{P}$. Solving Eq. 7 accounts for the long-range Coulombic interactions within the system, including the potential emergence of the so-called depolarization field that originates from the presence of unscreened charges on the polar surface. Parameter ϵ_b, sometimes called the background dielectric constant, represents contributions from core electrons to the dielectric response of the ferroelectric[13,14] that can moderately screen the polarization field. We choose $\varepsilon_b/\epsilon_0 = 10$ for PTO,[14] i.e., we use values that are close to those of the electronic contribution ϵ^∞ to the total dielectric permittivity.[13] Two things should be noted: varying this parameter does not seem to affect the results presented in this work and the electrostatic energy contribution tends to be three orders lower than the other energies at all times during the evolution in this particular analysis. The state of the dielectric substrate in contact with the FE layer is governed by a different set of equations. STO is assumed to be a linear dielectric, with an isotropic dielectric permittivity ϵ_m. The following equation must be satisfied for the electrostatic potential within the substrate:

$$\nabla \left(\epsilon_m \cdot \nabla \Phi \right) = 0, \tag{8}$$

complemented by the stress divergence equation:

$$\frac{\partial \sigma_{ij}}{\partial x_j} = 0. \tag{9}$$

The same governing equations exist in the vacuum region, except that $\mathbf{u}$ is nonexistent. The electrostatic potential boundary condition, $\Phi \to 0$, is enforced on the boundary planes of the vacuum (which are assumed to be far away from the layer). Consistency checks were done to make sure that, as a function of the size of the layer, the internal (fringing) electrostatic potential did in fact vanish

at the boundaries of the computational domain. Larger external vacuum domains were needed to ensure fringing fields from larger layers vanished. The elastic displacement field is required to vanish sufficiently far from the substrate/nanostructure interface (at about 25 nm depth). Variation of this depth does not appreciably affect the simulation energetics. Additionally, periodic boundary conditions are chosen along the x-axis to allow for computationally efficiency in simulating a very long patterned structure. Here, we set all variables $\boldsymbol{P}, \boldsymbol{u}$, and Φ *nodally* equivalent on the two boundary planes whose normals are parallel to $\pm y$-axis directions.

Our approach implemented in FERRET[9] allows for solving coupled Eqs. 5 through 6 self-consistently for the displacement vector field $\mathbf{u}(\mathbf{x})$, polarization vector field $\boldsymbol{P}(\mathbf{x}, t)$, and electro-static potential scalar field $\Phi(\mathbf{x})$. These equations are first separated into their respective subdomains, and then cast into the weak-form suitable for Galerkin's finite element method. A fully implicit time integration is implemented in a Newton-Raphson scheme. The iterative Generalized Minimal Residual[15] algorithm is used to solve the block (jacobi) diagonal preconditioned linear system. The full solve utilizes convergence to within 1×10^{-7} relative nonlinear residual tolerance at every time step.

Since Eq. 5 is a partial differential equation that depends on time, an initial condition for evolving the $\boldsymbol{P}$ field must be chosen. For this particular problem – to focus in on and understand the specific experimental results obtained – we adopt an initial condition that *biases* the polar field to produce aligned domain structures either aligned parallel or perpendicular to the milled boundary as the lowest total energy states found through evolution. After the initial condition is set, the temperature is then immediately set below T_C and the TDLGD Eq. 5 is evolved (by solving 7 and 6 at each time step) until a (local) energy minimum has been found. The simulation exit criterion is achieved when the difference in the magnitude of the total energy is below 0.1% during the two consecutive time steps.

1.4. Structure and materials

The computational domain of the problem is split into three volumes; a ferroelectric PTO volume atop a linear dielectric STO substrate surrounded by two vacuum blocks to model the empty space due to focused ion beam milling. The ferroelectric domain is meant to mimic the superlattice structure for reasons described in the main text. We assume a coherent interface between the ferroelectric and substrate materials blocks. We then discretize the total volume into a finite element model and the structure is meshed with hexahedral elements with CUBIT.[16] The resolution of the mesh is always such that there are 2-3 elements across the domain wall.

2. X-ray nanobeam analysis

2.1. Azimuthal angle δ as a function of $\Delta\Theta$

The domain diffuse scattering intensity forms a ring of intensity in a q_x-q_y-plane of reciprocal space with a radius of $2\pi/\Lambda$. Here Λ is the real-space domain period. Fig. S1 shows sections of reciprocal space in the q_x-q_y and q_x-q_z planes passing through the superlattice Bragg reflection. When the incident beam meets the superlattice Bragg condition the Ewald sphere intersects the ring of domain diffuse scattering intensity as shown in Fig. S1 (a). Other sections of the ring of diffuse scattering intensity can obtained by changing the x-ray incident angle by $\Delta\theta$ as shown in Fig. S1 (b). The magnitude of the reciprocal-space displacement Δx of the Ewald sphere along the q_x axis for an incident beam is:

$$\Delta x = r\cos\theta_2 - r\cos\theta_1.$$

The angles θ_1 and θ_2 are defined in Fig. S1(d). The azimuthal angle δ can be determined using:

$$\theta_1 = \theta_B + \Delta\theta,$$

$$\theta_2 = \sin^{-1}\left(\frac{z_2}{r}\right) = \sin^{-1}\left(\frac{z_0 - z_1}{r}\right) = sin^{-1}\left(2\sin\theta_B - \sin\theta_1\right),$$

and

$$\delta = \sin^{-1}\left(\frac{\Delta x}{2\pi/\Lambda}\right) = \frac{\Lambda}{\lambda}\left(\cos\left(\sin^{-1}\left(2\sin\theta_B - \sin\theta_1\right) - \cos\Theta_1\right)\right).$$

Note by using the following trigonometric identity, $\cos\sin^{-1}(\alpha) = \sqrt{1-\alpha^2}$, the expression for δ can be simplified to

$$\delta(\Delta\theta) = \frac{\Lambda}{\lambda}\left(\sqrt{1-\left(2\sin\theta_B - \sin\left(\theta_B + \Delta\theta\right)\right)^2} - \cos\left(\theta_B + \Delta\theta\right)\right),$$

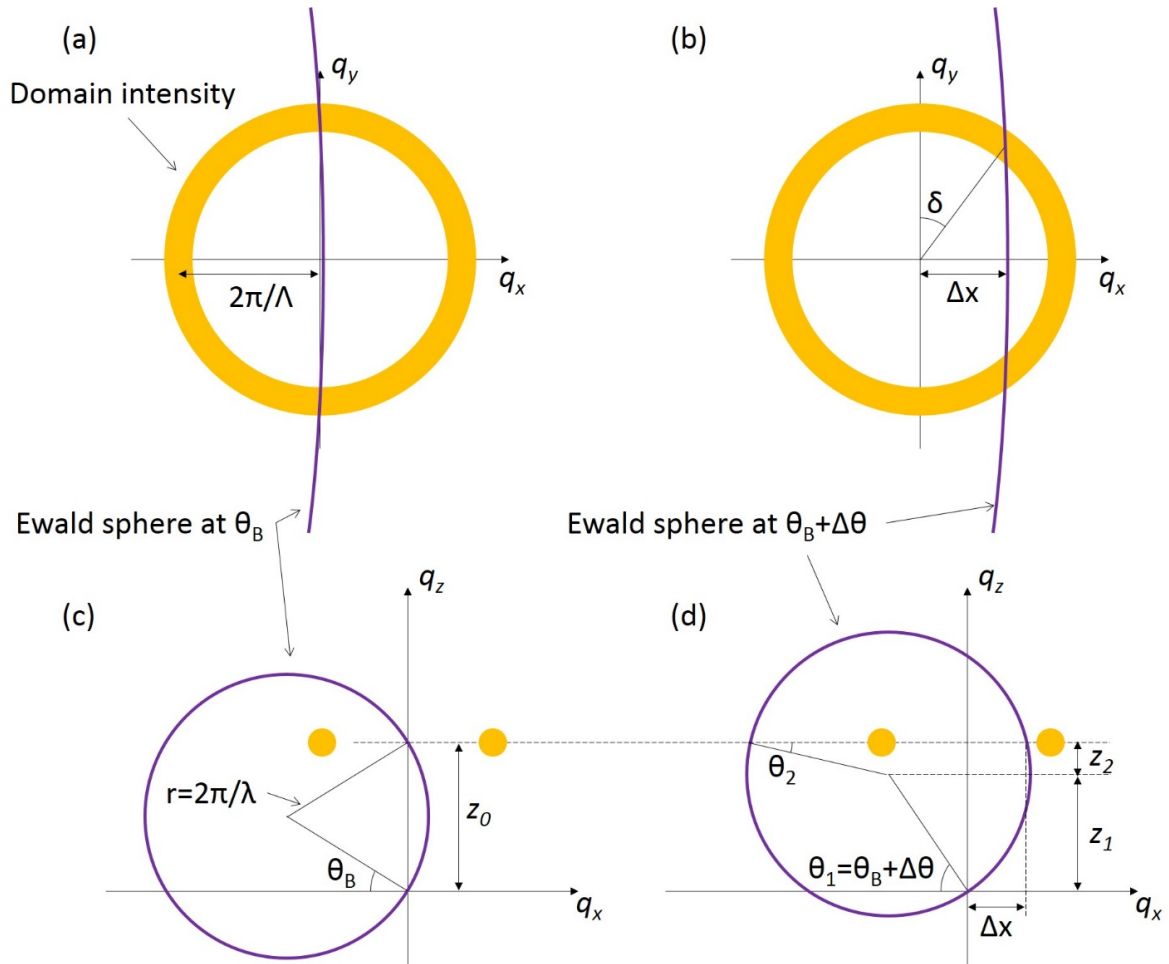with λ being the wavelength of the x-ray.

Figure S1: Reciprocal space maps with the Ewald sphere (purple) and the domain intensity (yellow). The superlattice Bragg peak is not shown. The corresponding x-ray incident angles are (a, c) θ_B and (b, d) $\theta_B + \Delta\theta$.

2.2. Strain measurement

2.2.1. Strain estimation using curvature

The magnitude of the strain resulting from the curvature of the nanostructure is in general difficult to determine because strain depends on the overall shape in addition to the curvature. We have obtained an order-of-magnitude estimate by assuming that the interface between the thin film and substrate is a neutral plane. The magnitude of the in-plane strain increases throughout the thickness of the film due to its curvature.

The curvature was measured by analyzing x-ray diffraction patterns for a series of locations across the width of the nanostructure. Under the diffraction conditions illustrated in the text, the curvature of the nanostructure across its width induces a shift in the diffracted intensity on the detector along a the direction perpendicular to the x-ray beam footprint by an angle $\Delta\chi$. The local tilt of the planes $\Delta\alpha$ is calculated from the angular shift of diffraction patterns using the relationship $\Delta\alpha = \frac{1}{2sin(\theta_B)}\Delta\chi$. The curvature is obtained using the numerical derivative of the orientation of the planes as a function of position. The curvature in the 800-nm-wide nanostructure discussed in the main text is 5880 m^{-1}, corresponding to a radius of curvature of 0.17 mm. The average in-plane structural strain is defined as $t/2R$, where t is the film thickness and R is the radius of curvature. The in-plane strain for this curvature is 0.03%, corresponding to an out-of-plane strain of -0.01%.

2.2.2. Out-of-plane strain measurement using x-ray nanodiffraction

The (002) Bragg reflection of the PTO/STO superlattice appears on the detector under diffraction conditions in which the (002) planes meet the Bragg condition. The nanodiffraction experiment employs a highly convergent focused x-ray beam. The planes thus meet the Bragg condition for all angles within the range spanned by the convergence angle of the focused x-ray nanobeam.

Fig. S2 shows a set of diffraction patterns acquired along the length of a 500-nm-wide nanostructure, following the path indicated by the green line. The vertical axis of the diffraction patterns corresponds to the conventional 2θ scattering angle. All of the patterns were acquired at a nominal

10

x-ray incident angle $0.03\,\mathrm{deg}$ less than the Bragg angle in the unpatterned regions. The diffraction patterns numbered 1, 2, 3, 4, 9, 10, 11, and 12 in Fig. S2 were acquired outside of the nanostructure. Diffraction patterns numbered 5, 6, 7, and 8 were acquired within the nanostructure.

The diffracted intensity associated with the PTO/STO 002 Bragg reflection appears as a region of high intensity the detector. The 2θ angles of the PTO/STO 002 Bragg reflection were calculated in each image using the centroid of the intensity distribution along the 2θ angular axis. The Bragg reflection intensities in the diffraction patterns acquired within the nanostructure appear at a value of 2θ that is $0.017\,\mathrm{deg}$ larger than in the diffraction patterns acquired outside of the nanostructure. This angular difference (Δ) arises because the out-of-plane lattice parameter within the nanostructure is smaller than in the unpatterned region. The angular difference can be used to calculate the out-of-plane strain (ϵ_z) using $\epsilon_z = -\cot(\Theta_B)\,\Delta$. The resulting strain is $\epsilon_z = $ -0.08 %. Note that this is the same order of magnitude as the value obtained using the curvature.
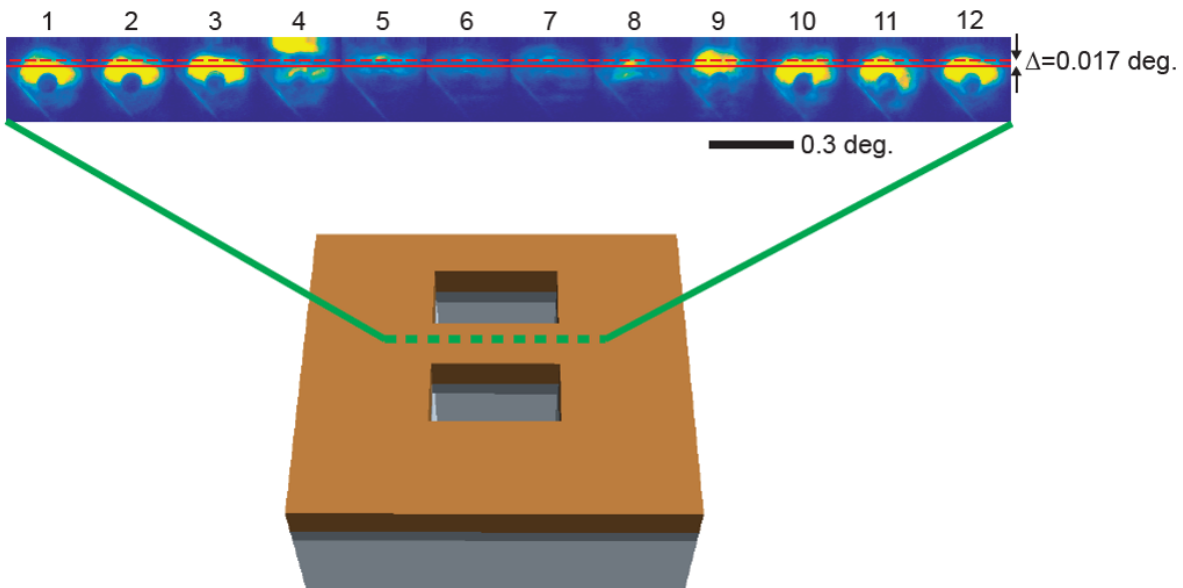

Figure S2: Diffraction patterns acquired along the length of a 500-nm-width nanostructure along the path indicated by the green dotted line

References

(1) Li, Y. L.; Hu, S. Y.; Liu, Z. K.; Chen, L.-Q. *Appl. Phys. Lett.* **2001**, *78*, 3878.

(2) Li, Y. L.; Hu, S. Y.; Liu, Z. K.; Chen, L.-Q. *Appl. Phys. Lett.* **2002**, *81*, 427.

(3) Lu, H., X. Li; Cao, W. *J. Appl. Phys.* **2013**, *114*, 224106.

(4) Nye, J. F. *Physical Properties of Crystals*; Oxford University Press Inc., 1985.

(5) Jain, A.; Ong, S. P.; Hautier, G.; Chen, W.; Richards, W. D.; Dacek, S.; Cholia, S.; Gunter, D.; Skinner, D.; Ceder, G.; Persson, K. A. *APL Mater.* **2013**, *1*, 011002.

(6) de Jong, M.; Chen, W.; Angsten, T.; Jain, A.; Notestine, R.; Gamst, A.; Sluiter, M.; Ande, C. K.; van der Zwaag, S.; Plata, J. J.; Toher, C.; Curtarolo, S.; Ceder, G.; Persson, K. A.; Asta, M. *Scientific Data* **2015**, *2*, 150009.

(7) Rabe, K. M.; Ahn, C. H.; Triscone, J.-M. *Physics of Ferroelectrics: A Modern Perspective*; Springer-Verlag, Berlin, 2007.

(8) Müller, K. A.; Burkard, H. *Phys. Rev. B* **1979**, *19*, 3593.

(9) The FERRET code-repository is developed within the open-source MOOSE environment[10] and is available at https://bitbucket.org/mesoscience/ferret.

(10) Gaston, D.; Newman, C.; Hansen, G.; Lebrun-Grandié, D. *Nucl. Eng. Des.* **2009**, *239*, 1768.

(11) Meng, Q.; Han, M.-G.; Tao, J.; Xu, G.; Welch, D. O.; Zhu, Y. *Phys. Rev. B* **2015**, *91*, 054104.

(12) Li, Y.; Hu, S.; Liu, Z.; Chen, L. *Acta Mater.* **2002**, *50*, 395.

(13) Baroni, S.; Gironcoli, S.; Corso, A. D. *Rev. Mod. Phys.* **2001**, *73*, 515.

(14) Hlinka, J.; Marton, P. *Phys. Rev. B.* **2006**, *74*, 104104.

(15) Saad, Y.; Schultz, M. *J. Sci. Stat. Comp.* **1986**, *7*, 856.

(16) CUBIT meshing software is developed by Sandia National Laboratories and is available at https://cubit.sandia.gov/.